RSC Advances

PAPER

View Article Online
View Journal | View Issue

Cite this: *RSC Adv.*, 2022, **12**, 4153

Hollow terbium metal–organic-framework spheres: preparation and their performance in Fe^{3+} detection†

Xiaozhan Yang, *[ab] Yicun Liang,[a] Wenlin Feng,[ab] Chaolong Yang,[c] Lian Wang,[d] Guojia Huang[e] and Daoyuan Wang[f]

Received 4th November 2021
Accepted 22nd January 2022

DOI: 10.1039/d1ra08088a

rsc.li/rsc-advances

Hollow metal–organic framework (MOF) micro/nanostructures have been attracting a great amount of research interest in recent years. However, the synthesis of hollow metal–organic frameworks (MOFs) is a great challenge. In this paper, by using 1,3,5-benzenetricarboxylic acid (H_3BTC) as the organic ligand and 2,5-thiophenedicarboxylic acid (H_2TDC) as the competitive ligand and protective agent, hollow terbium MOFs (Tb-MOFs) spheres were synthesized by a one-pot solvothermal method. By comparing the morphology of Tb-MOFs in the presence and absence of H_2TDC, it is found that H_2TDC plays a key role in the formation of the hollow spherical structure. Single crystal analyses and element analysis confirm that H_2TDC is not involved in the coordination with Tb^{3+}. Interestingly, Tb-MOFs can be used as the luminescent probes for Fe^{3+} recognition in aqueous and *N*,*N*-dimethylformamide (DMF) solutions. In aqueous solution, the quenching constant (K_{SV}) is 5.8×10^{-4} M^{-1}, and the limit of detection (LOD) is 2.05 μM. In DMF, the K_{SV} and LOD are 9.5×10^{-4} M^{-1} and 0.80 μM, respectively. The sensing mechanism is that the excitation energy absorption of Fe^{3+} ions reduces the energy transfer efficiency from the ligand to Tb^{3+} ions.

1. Introduction

Due to their enhanced surface-to-volume ratio, micro-reactor environment, high loading capacities, excellent designability and flexibility, hollow metal–organic frameworks (MOFs) have shown fascinating physicochemical properties and wide applications, especially in molecule adsorption, filtration, diffusion and transfer.[1–3] Recently, several strategies have been developed to synthesize hollow MOFs, such as template-mediated assembly, interfacial synthesis, stepped dissolution-regrowth, ion-exchange reactions, chemical etching, *etc.*[4–6] Using carboxylate modified polystyrene spheres as a hard template, hollow zeolitic imidazolate framework-8 (ZIF-8) microspheres were fabricated by electrostatic interaction.[7] Choe *et al.* prepared single-shell and double shelled MOFs using metal organic polyhedra as a self-template and building block.[8] Wang *et al.* synthesized a hollow zirconium-porphyrinic MOF with single atoms embedded using benzoic acid as a competitive reagent.[9] By adding carbon dioxide bubbles into continuous ionic liquid to form a liquid–gas interface, hollow Zn-BTC was successfully prepared.[10] Hollow MOFs can also be obtained through liquid–liquid interface and solid–liquid interface methods.[11–13] Although great achievements have been achieved, the synthesis of hollow MOFs with controllable structure is still a complicated and difficult task; it is urgently needed to synthesize hollow MOFs with a simple and easy method.[3,4]

The Fe^{3+} ion is one of the essential metal ions in industrial production and biological systems; a deficiency of Fe^{3+} ions in the human body will cause physical problems such as anemia, liver injury, diabetes, and heart failure. But excessive Fe^{3+} will cause serious environmental issues.[14–16] Therefore, the simple, rapid and selective detection of Fe^{3+} ions is meaningful to research. Due to the advantages of high sensitivity, good stability, simple operation and real-time detection, a luminescent quenching-type sensor is often considered to be an ideal choice for high-sensitivity and high-precision Fe^{3+} ion detection.[17,18] Lanthanide metal–organic frameworks have high luminous efficiency, high color purity, large Stokes-shift, long luminescence life, and have been widely used in the selective detection of metal ions and small molecules.[18–20]

[a]*School of Science, Chongqing University of Technology, China*

[b]*Chongqing University of Technology, Chongqing Key Laboratory of Green Energy Materials Technology and Systems, China. E-mail: xiaozhan@126.com*

[c]*School of Materials Science and Engineering, Chongqing University of Technology, China*

[d]*Guangzhou Special Pressure Equipment Inspection and Research Institute, China*

[e]*Department of Department of Medical Research, Guangdong Provincial People's Hospital, Guangdong Academy of Medical Sciences, China*

[f]*Department of Chemistry and Physics, University of Arkansas at Pine Bluff, USA*

† Electronic supplementary information (ESI) available: Crystal data, powder X-ray diffraction patterns (PXRD), TGA curves, SEM images, emission spectra and sensing performance (PDF). CCDC 2082489. For ESI and crystallographic data in CIF or other electronic format see DOI: 10.1039/d1ra08088a

Thus, in this work, novel hollow spherical Tb-MOFs were prepared easily by the solvothermal method based on 1,3,5-benzenetricarboxylic acid (H_3BTC) as the ligand, and 2,5-thiophenedicarboxylic acid (H_2TDC) as the competitive and protective agent. The crystal structure, morphology, elemental information, thermal stability and luminescent properties of the Tb-MOFs were characterized and analyzed, and the sensing performance of Fe^{3+} ions is evaluated and discussed in detail.

2. Experimental section

2.1 Reagents

H_3BTC (98%), H_2TDC (98%) and terbium nitrate hexahydrate ($Tb(NO_3)_3 \cdot 6H_2O$, 99.9%) were purchased from Macklin Inc. Ferric nitrate nonaqueous ($Fe(NO_3)_3 \cdot 9H_2O$, A.R.) and *N*,*N*-dimethylformamide (DMF, A.R.) were obtained from Aladdin. All reagents were not further purified before use.

2.2 Instruments

The single crystal diffraction data were recorded by Bruker D8 Advance X-ray diffractometer with Ga Kα radiation. Powder X-ray diffraction (XRD) patterns were measured on a PANalytical Empyrean Series 2 diffractometer (Cu K_α) in the 5–50° angular range with a step of 0.026° and a scanning speed of 7° per minute. Thermogravimetric analysis (TGA) was performed under a flow of N_2 in the temperature range 10–700 °C at a heating rate of 10 °C min^{-1} on a TGA Q-50 thermogravimetric analyzer. The UV-Vis absorption and luminescence spectra were determined on a UV 3600 spectrometer (Shimadzu, Japan) and an F-4600 fluorescence spectrometer (Shimadzu, Japan), respectively. The emission decay processes and quantum yields were recorded on an FLS980 spectrofluorometer system (Edinburgh, UK). Morphology analysis was obtained using a field emission scanning electron microscope (FE-SEM, JSM-7800F, Japan, LaB6, ZEISS, Germany). The X-ray photoelectron spectroscopy (XPS) was collected on an XPS-Theta probe instrument (Escalab250Xi, Thermo Fisher, USA). The high-resolution transmission electron microscope (HRTEM) with high-angle annular dark field (HAADF, ThermoFisher Scientific Talos F200S, Czech Republic) was used to analyze the element distribution and composition of the Tb-MOFs. Fourier-transform infrared spectroscopy (FTIR) measurements were recorded using an FTIR spectrometer (iS50, Nicolet, USA).

2.3 Synthesis of Tb-MOFs

1 mmol (0.453 g) $Tb(NO_3)_3 \cdot 6H_2O$, a certain proportion of H_3BTC and H_2TDC (Table S4, ESI†) were dissolved in 10 ml DMF, respectively. The above three solutions were fully mixed and transferred to a Teflon-lined reactor and heated at 150 °C for 72 h. The reaction products were centrifuged and cleaned with DMF, and the Tb-MOFs were obtained after drying in a vacuum drying oven at 60 °C.

3. Results and discussion

3.1 Structure of Tb-MOFs

The single-crystal X-ray diffraction analysis results of Tb-MOFs are shown in Tables S1–S3, ESI.† Tb-MOFs are assigned to the monoclinic space group *C*2/*c* with the lattice parameters of a = 18.6318(8) Å, b = 18.6318(8) Å, c = 19.7386(8) Å. Both H_3BTC and DMF are participated in the coordination, forming a three-dimensional MOFs structure with Tb^{3+} as the center, while H_2TDC does not coordinate with Tb^{3+}.

The synthesis flow chart of Tb-MOFs is shown in Fig. S1, ESI.† Hollow sphere Tb-MOFs are synthesized using H_3BTC and Tb^{3+} in the DMF system under the action of H_2TDC. In this process, both H_3BTC and DMF participated in the synthesis of Tb-MOFs structure. The coordination environment of Tb^{3+} is shown in Fig. 1a, Tb01 is 8-coordinated environment consisting of 6 oxygen atoms from H_3BTC (H_3BTC1, H_3BTC2, H_3BTC3) anion and 2 oxygen atoms from DMF (DMF1, DMF2, DMF3). As shown in Fig. S2, ESI,† O002 and O005 from H_3BTC1 are coordinated with Tb^{3+} by asymmetric chelation, the Tb–O bond lengths are 2.443(4) Å and 2.399(4) Å, respectively, and the bond angle of Tb–O–Tb is 54.30(12)°. O009 and O006 in H_3BTC2 are coordinated with Tb^{3+} by symmetric chelation, the Tb–O bond lengths are 2.413(4) Å and 2.415(4) Å, respectively, and the bond angle of Tb–O–Tb is 53.61(14)°. O003 and O004 in H_3BTC3 and H_3BTC4 coordinate with Tb^{3+} by bridging, and the Tb–O bond lengths are 2.330(4) Å and 2.283(4) Å, respectively. O007 and O008 monodentate coordination Tb^{3+} from DMF1 and DMF2, the bond lengths of Tb–O are 2.379(5) Å and 2.354(4) Å, respectively. In the whole coordination structure, the bond angle of O–Tb–O ranges from 53.61(14)° to 156.56(14)°.

So each local asymmetric unit in the cell contains one Tb^{3+}, four H_3BTC anions and two DMF molecules (Fig. 1b). Each structural unit cell contains two local asymmetric units, each local asymmetric unit contains 1 Tb^{3+}, four H_3BTC anions and two DMF molecules. Each of the two asymmetric units forms a Tb binuclear structure. The chain connection between the two dual-core structures forms a two-dimensional planar structure (Fig. 1c). The two-dimensional plane structure forms a stable three-dimensional frame structure with micropores through the cross-layer connection form (Fig. 1d).

3.2 XRD, TG, SEM, FTIR and element analyses

The XRD pattern of Tb-MOFs (CCDC 2082489, Fig. S3, ESI†) shows that Tb-MOFs have good crystallinity, and the TG curve (Fig. S4, ESI†) indicates that Tb-MOFs have good thermal stability. The comparative morphologies of Tb-MOFs with and without H_2TDC are shown in Fig. 2a and b. It is found that Tb-MOFs without H_2TDC are self-assembled into stable rod bundles, while the addition of H_2TDC leads to forming the hollow sphere structure. The hollow structure is very stable and ultrasonic treatment for 30 minutes can't damage the hollow structure. SEM morphology of Tb-MOFs prepared with different H_3BTC/H_2TDC ratios (Fig. S5, ESI†) indicates that the hollow sphere structure is not changed by different H_3BTC/H_2TDC ratios. These results indicate that H_2TDC is not only

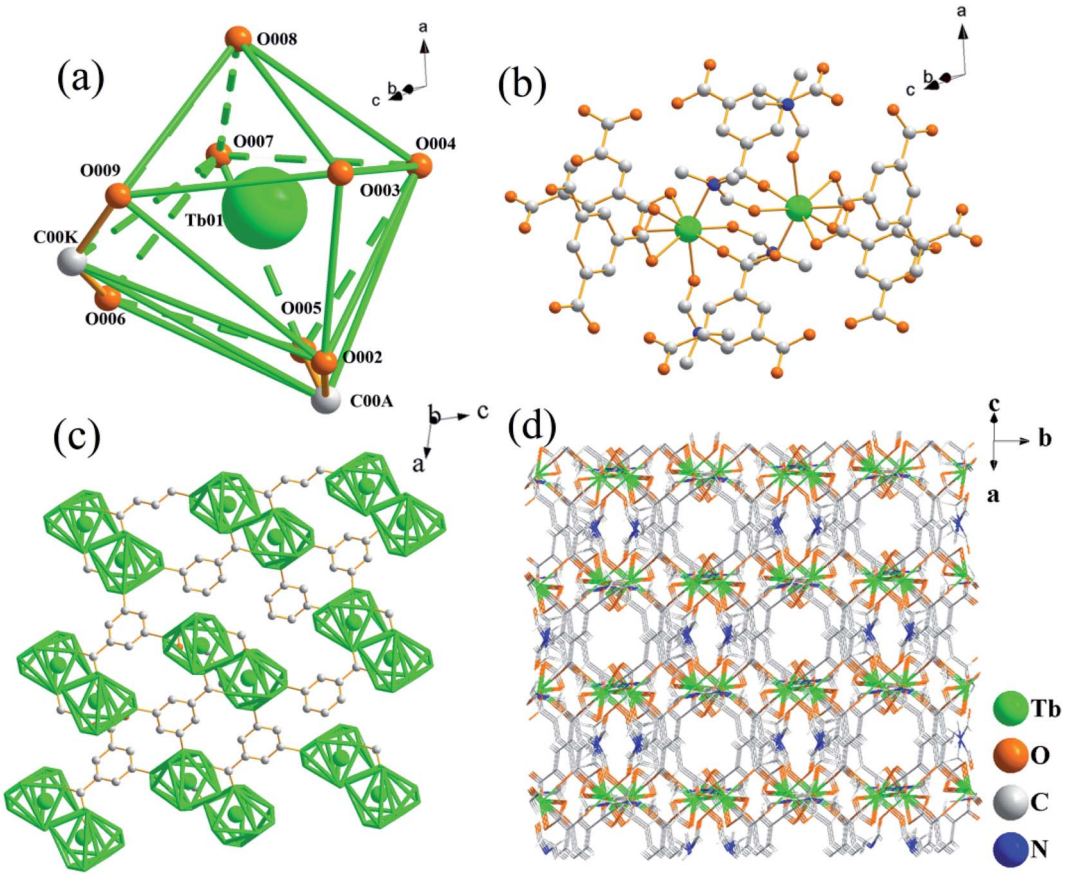

Fig. 1 (a) Coordination environment of Tb atom. (b) Single crystal structure of Tb-MOFs. (c) Two-dimensional frame diagram of Tb-MOFs. (d) Three-dimensional frame diagram of Tb-MOFs.

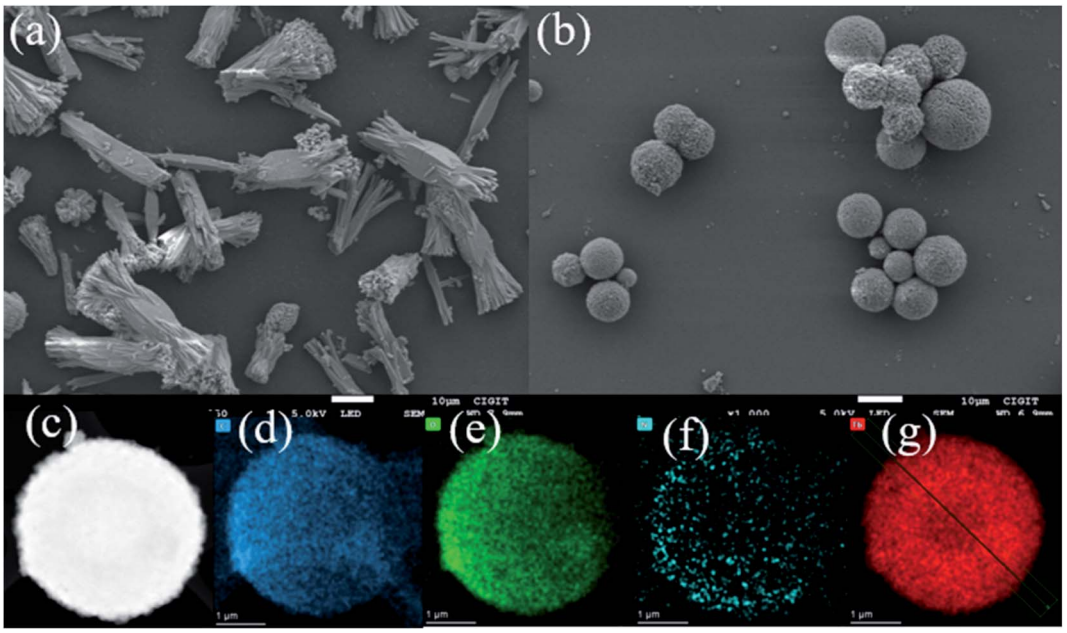

Fig. 2 (a) SEM image of Tb-MOFs without H_2TDC. (b) SEM image of Tb-MOFs with H_2TDC. (c) HAADF image of Tb-MOF with H_2TDC. (d)–(g) mapping images of C, O, N and Tb element, respectively.

a competitive reagent but also a protective agent. High-angle annular darkfield (HAADF) and element mappings (C, O, N and Tb) analysis of Tb-MOFs are respectively shown in Fig. 2c–g, which indicate that these elements are distributed uniformly throughout the whole sphere. The Tb-MOFs are consistent with that of the single crystal. The shadow in the sphere center of Tb element indicates that Tb-MOFs are hollow spheres (Fig. 2g). The line scanning profile of Tb element distribution (Fig. S6, ESI†) indicates that there are fewer elements in the center of the sphere, which further confirms that it is a hollow spherical structure.

As shown in Fig. 3, Tables S5 and S6,† no sulfur can be detected in all samples during the preparation process and the final sample, which confirms that H_2TDC was not involved in the coordination with Tb^{3+}. So the formation mechanism of hollow spherical Tb-MOF is deduced as follows. In the initial stage, H_2TDC serves as the coordination competitor. Due to the coordination ability between H_3BTC and Tb^{3+} being stronger than that of H_2TDC, the surface-energy-driven mechanism may be responsible for the crystallization process,[21] forming solid spheres stacked by Tb-BTC nanoblocks (1–2 h in Fig. 3a). In the second stage, many defects exist in the inner region of the solid spheres, such as incomplete coordination metal nodes and grain boundaries, which makes the solid spheres unstable. In addition, the concentration of H_3BTC decreases due to the participation in coordination, while the concentration of H_2TDC does not change. The rich carboxyl groups on H_2TDC surface can provide protons and participate in competitive chelation with Tb^{3+}, partially destroying the formed coordination bond. With the dissolution of the original unstable coordination and the formation of new coordination, the solid sphere structure collapsed (3 h in Fig. 3a) to form the hollow structure (4–6 h in Fig. 3a). This deduction is proved by the elemental data in Table S5, ESI.† In the third stage, the protons released by H_2TDC not only penetrate the hollow core but also cover the surface of the spheres, shielding the formed coordination bonds. Finally, a stable hollow spherical structure is formed (Fig. S5†). Therefore, H_2TDC serves as a competitive ligand and protective agent during the synthesis of Tb-MOF.

The FTIR spectrum of the Tb-MOFs is shown in Fig. 3b. The characteristic band 650–900 cm^{-1} was due to the out-plane bending vibration of C–H in benzene ring of Tb-MOFs. The peak at 918 cm^{-1} can be attributed to the out-plane bending vibration of hydroxyl group. Peaks at 1626 cm^{-1} and 1434 cm^{-1} (or 1568 cm^{-1} and 1375 cm^{-1}) are attributed to the asymmetric and symmetric stretch vibration of COO^- group ($\nu_{as}(COO^-)$ and $\nu_s(COO^-)$), respectively. These results indicate that the carboxylic groups of H_3BTC are dehydrogenated and then coordinated with Tb^{3+} ions in Tb-MOF.[22] The difference between $\nu_{as}(COO^-)$ and $\nu_s(COO^-)$ value is 192 cm^{-1} (or 193 cm^{-1}), which implies that three coordinate modes, monodentate, chelation and bridging exist in the synthesized Tb-MOF.[22]

3.3 Luminescence properties

The emission spectra of Tb-MOFs with different ratios of H_3BTC and H_2TDC using the excitation wavelength of 320 nm are shown in Fig. S7, ESI.† In the luminescence process, H_3BTC serves a sensitizer to enhance the luminescence of Tb-MOFs. When H_3BTC/H_2TDC ratio is 1 : 1, the synthesized Tb-MOFs have fewer coordination defects, H_3BTC can transfer the absorbed energy to Tb-MOFs easily which promotes the luminescence of Tb-MOFs. While H_3BTC/H_2TDC ratios are other values, some uncoordinated Tb^{3+} and carboxyl groups hinder the energy transfer from H_3BTC to Tb^{3+}. Thus, Tb-MOFs with the ratio of H_3BTC/H_3TDC of 1 : 1 have the strongest luminescence intensity. Four emission peaks at 488 nm, 545 nm, 584 nm and 621 nm are corresponding to the $^5D_4 \rightarrow {}^7F_J$ ($J = 6, 5, 4, 3$) transitions of Tb^{3+}, respectively. Therefore, Tb-MOFs with the H_3BTC/H_2TDC ratio of 1 : 1 are synthesized for further exploration.

3.4 Sensing performance of Tb-MOFs to Fe^{3+}

2 mg Tb-MOFs was, respectively, mixed evenly in 1×10^{-3} mol L^{-1} $M(NO_3)_n$ (M = Ca^{2+}, Cr^{3+}, NH_4^+, Ba^{2+}, Zn^{2+}, Mn^{2+},

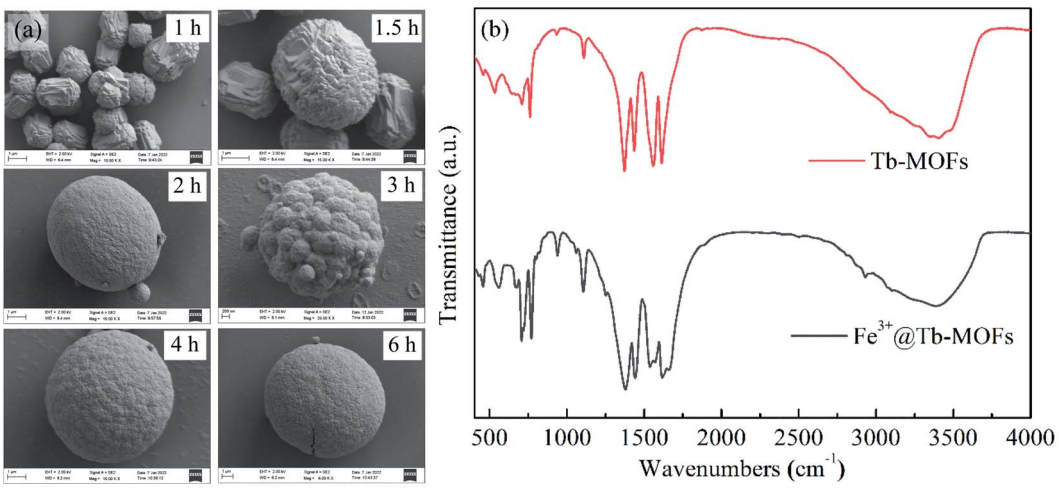

Fig. 3 (a) SEM images for 1 h, 1.5 h, 2 h, 3 h, 4 h, 6 h during Tb-MOFs preparation. The synthesis process of Tb-MOFs hollow spheres. (b) FTIR spectra of Tb-MOFs and Fe^{3+}@Tb-MOFs.

Co^{2+}, Bi^{3+}, Ag^{+}, Cu^{2+}, Fe^{2+}, Fe^{3+}) aqueous solutions, and then the suspended solutions of different metal ions were obtained. Before photoluminescence (PL) performance measurements, the suspensions were treated with ultrasonication for 10 minutes. The PL properties are recorded and compared in Fig. 4a. Obviously, expected for Fe^{3+} solution, other cations display a little influence on the emission spectra of Tb-MOFs, while the emission intensities decreased rapidly in Fe^{3+} solution. Then, when multiple metal ions exist in aqueous solution at the same time, the selectivity to Fe^{3+} has been investigated (Fig. S9, ESI†). When there are 1, 3, 5, 7, and 9 metal ions in an aqueous solution at the same time, it still has good selectivity to Fe^{3+}. Therefore, Tb-MOFs can be used as a luminescent sensor for Fe^{3+} ions detection.

To clarify the quenching behaviors of Tb-MOFs to Fe^{3+} ions in detail, the concentration-dependent emission measurements were carried out (Fig. 4b). With the increasing concentration of Fe^{3+} ions, the luminescence intensities of Tb-MOFs gradually decreased, when the concentration of Fe^{3+} ions is 150 μM, the luminescence is almost completely quenched.

The fitting curve between the luminescence intensity of Tb-MOFs at 545 nm *versus* the concentration of Fe^{3+} is shown in Fig. 4c. With the increase of Fe^{3+} concentration in the range of 0–150 μM, the luminescence intensities decrease exponentially which satisfies the functional relationship $y = 526.8\exp(-x/6.3) + 1014.5\exp(-x/89.9) - 176.4$, and the fitting parameter $R^2 = 0.9981$. The inset shows that there is a good linear relationship between the luminescence intensities and the Fe^{3+} concentrations (0–10 μM), which satisfies $y = 1335.7 - 55.8x$ with the linearity of $R^2 = 0.9974$. The limit of detection (LOD) of Tb-MOFs for Fe^{3+} can be calculated by,[23]

$$S_b = \sqrt{\frac{\sum (F - F_0)^2}{N - 1}}, \quad \mathrm{LOD} = \frac{3S_b}{S} \tag{1}$$

where N is the number of blank groups measured without Fe^{3+} ($N = 20$), F_0 is the luminous intensity of the sample in aqueous solution, F is the average value of F_0, and S_b ($S_b = 49.7$) is the standard deviation of 20 blank groups, S is the slope of the curve in the Fe^{3+} concentration range of 0–10 μM in the inset of Fig. 4c ($S = 55.8$), substituting the above values to calculate the detection limit of Fe^{3+} for Tb-MOFs samples in aqueous solution is about 2.05 μM. Further, the quenching efficiency of Tb-MOFs to Fe^{3+} can be evaluated by the Stern–Volmer[24] equation,

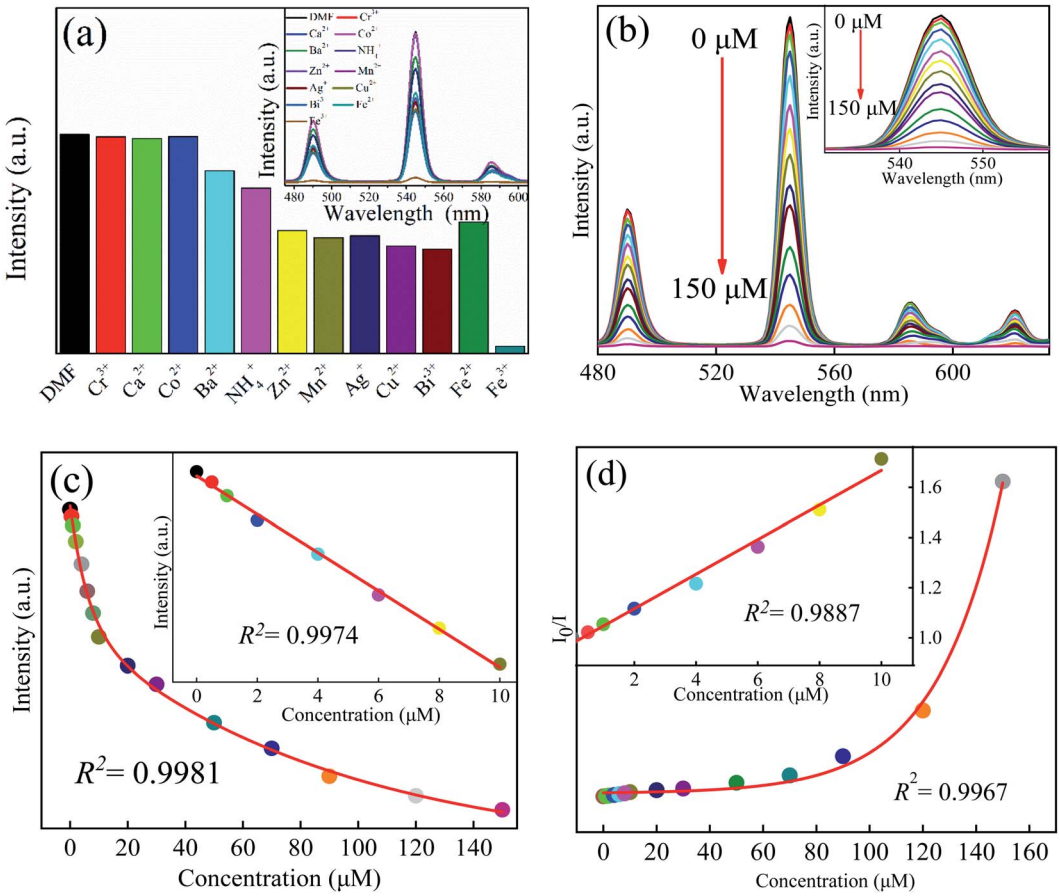

Fig. 4 (a) Histogram of Tb-MOFs luminescence intensities in aqueous solutions with different metal ions (at 545 nm), and the inset is emission spectra. (b) Emission spectra of Tb-MOFs in various concentrations of Fe^{3+} solutions, and the inset is emission spectra near 545 nm. (c) Fitting curves of luminescence intensities of Tb-MOFs *versus* Fe^{3+} concentrations (0–150 μM), and the inset is luminescence intensities *versus* low Fe^{3+} concentration (0–10 μM). (d) Stern–Volmer fitting curve (Fe^{3+} concentration: 0–150 μM), and the inset is Stern–Volmer fitting curve at low (Fe^{3+} concentration: 0–10 μM).

$$\frac{I_0}{I} = 1 + K_{SV}[M] \quad (2)$$

where I_0 and I are the relative PL intensities before and after incorporation of the analyte, $[M]$ is the molar concentration of the Fe^{3+}, and K_{SV} is the Stern–Volmer quenching constant. As illustrated in inserted Fig. 4d, the Stern–Volmer quenching curve for Fe^{3+} shows a good linear relationship $y = 0.98 + 0.07x$ at low concentration (0–10 μM) with a linear fit correlation coefficient of 0.9887. From the inset of Fig. 4d, the K_{SV} (5.8×10^{-4} M^{-1}) value can be obtained, suggesting a strong quenching effect of Fe^{3+} on Tb-MOFs. However, the increase in concentration (10–150 μM) leads to the curve deviation from the linear relation (Fig. 4d), and a good exponential relationship $y = 0.11\exp(-x/24.61)+1.49$ can be obtained with the fitting parameter of $R^2 = 0.9967$.

In addition, the sensing properties of Tb-MOFs to different metal ions in DMF solvents were also evaluated. The research method is the same as those in aqueous case. Tb-MOFs still have good selectivity to Fe^{3+} in the DMF system (Fig. S9, ESI†). Continue to explore the sensitivity test of Tb-MOFs to Fe^{3+} in DMF (Fig. S10, ESI†). Interestingly, Tb-MOFs also show a good specific recognition ability to Fe^{3+}. The LOD is about 0.80 μM, and the Stern–Volmer quenching constant K_{SV} is 9.5×10^{-4} M^{-1}. These results indicate that Tb-MOFs can act as an excellent luminescent sensing material for Fe^{3+} ion detection.

In general, the luminescence quenching mechanism of the MOFs can be mainly summarized as three kinds: ion exchange, structural collapse or change, photon absorption competition between adsorbed ions and MOFs,[25] In order to fully explain the luminescent quenching mechanism of Fe^{3+} to Tb-MOFs, the following four measurements are carried out. First, the XRD patterns of Tb-MOFs and Fe^{3+}@Tb-MOFs measurement results are shown in Fig. S3, ESI,† the Tb-MOFs and Fe^{3+}@Tb-MOFs display similar XRD pattern characteristics, which excludes the possibility of MOFs skeleton collapse or change. Second, before and after Fe^{3+} adsorption, XPS curves of the Tb-MOFs and Fe^{3+}@Tb-MOFs (Fig. 5a) show that no obvious variation occurs in the positions of the element binding energy, only a weak characteristic peak of Fe^{3+} (710.8 eV) appears in the XPS curve of Fe^{3+}@Tb-MOFs. The binding energy positions of Tb 3d remain unchanged (Fig. 5b), which indicates that the coordination environment of Tb atom does not change before and after adsorption of Fe^{3+}, and there is no ion exchange between Fe^{3+} and Tb^{3+}. Broadening and splitting of carboxyl characteristic peaks in FTIR spectrum of Fe^{3+}@Tb-MOF (Fig. 3b) proves that Fe^{3+} affected the coordination environment of the carboxyl

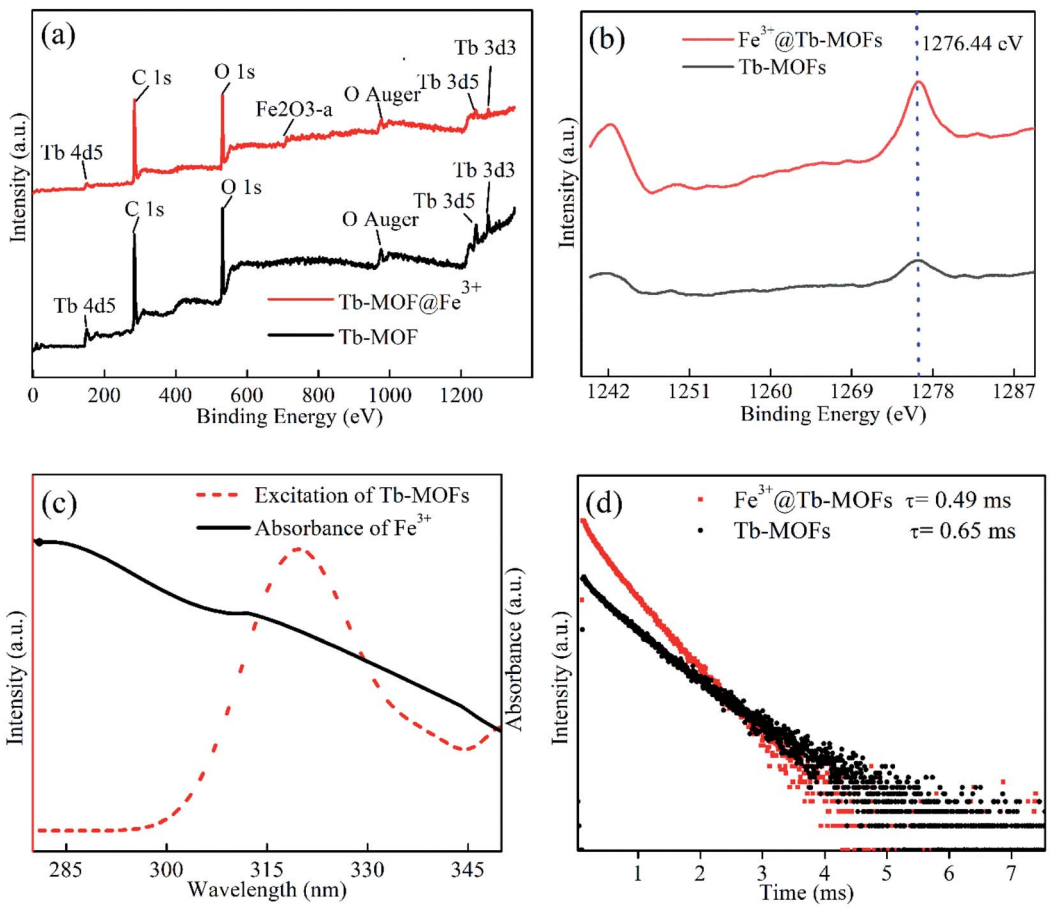

Fig. 5 (a) XPS spectra of Tb-MOFs and Fe^{3+}@Tb-MOFs. (b) Tb 3d XPS curves of Tb-MOFs and Tb–Fe^{3+}@Tb-MOFs. (c) UV-Vis spectrum of Fe^{3+} and excitation spectrum of Tb-MOFs, (d) Luminescence lifetime of Tb-MOFs and Fe^{3+}@Tb-MOFs.

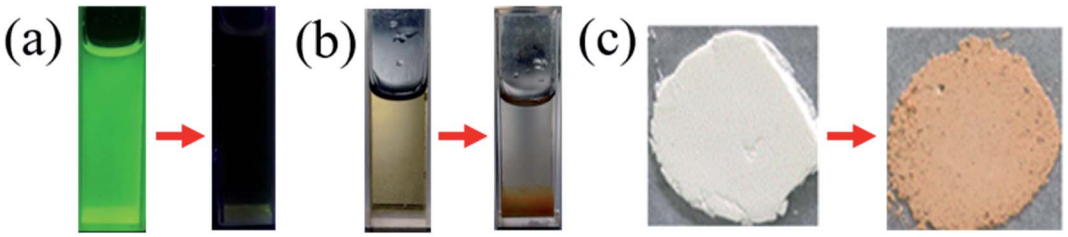

Fig. 6 (a) Photographs of Tb-MOFs suspension (left) and Fe^{3+} (right) under 365 nm illumination. (b) Photographs of Fe^{3+} before (left) and after (right) addition of Tb-MOFs. (c) Photographs of Tb-MOFs powder before (left) and after (right) adsorption of Fe^{3+}.

Table 1 Comparisons of the sensing parameters with other Tb^{3+} based MOF for Fe^{3+} sensing

MOF	K_{SV} (M^{-1})	LOD (μM)	Detection range (μM)	Ref.
$[Tb(cpia)(H_2O)_2]_n \cdot nH_2O$	1.2×10^4	2.06	0–120	30
Tb^{3+} with H_4ddb	7.64×10^4	0.936	33–330	31
$[Tb(C_5H_7O_4)(C_5H_6O_4)(H_2O)_2]_n$	8.07×10^4	—	0–100	32
$H_3O[Tb\text{-}(L\text{-}N)(H_2O)_2] \cdot 2H_2O$	7.93×10^3	—	0–250	33
$[Tb_3(L\text{-})_2(HCOO)(H_2O)_4] \cdot 6H_2O$	1.39×10^4	—	0–400	
$[Tb(tftba)_{1.5}(phen)(H_2O)]_n$	4.043×10^4	12.7	0–800	34
Tb-MOF	5.8×10^4	2.05 in water	0–150	This work
	9.5×10^4	0.8 in DMF	0–150	

group. Third, the UV-Vis absorption spectrum of Fe^{3+} and the excitation spectrum of Tb-MOFs are shown in Fig. 5c, the major degree overlap demonstrates that the excitation energy can be effectively absorbed by Fe^{3+}, and the energy transfer efficiency from organic ligands to Tb^{3+} ions will be reduced and the luminescence quenching occurs.[26,27] In Fig. 5d, the luminescence lifetime of Tb-MOFs is about 0.65 ms, and that of Fe^{3+}@Tb-MOFs is about 0.49 ms, the reduced lifetime further confirms the existence of the energy transfer in Fe^{3+}@Tb-MOFs.[28,29] These results indicate that the co-existence of absorption competition and energy transfer should be responsible for the quenching mechanism.

Due to the hollow spherical structure, the large specific surface area of Tb-MOFs, the adsorption performance of Tb-MOFs to Fe^{3+} are also evaluated. 500 μM Fe^{3+} aqueous solution was added to the aqueous suspension of Tb-MOFs, and the results are shown in Fig. 6a. After Fe^{3+} was added to Tb-MOFs suspension, the luminescence of Tb-MOFs was quenched, the original yellow Fe^{3+} solution turned into a colorless transparent solution (Fig. 6b), and the original white Tb-MOFs powder changed into yellow (Fig. 6c). Combined with the above quenching mechanism analysis, it can be concluded that the hollow Tb-MOFs can not only adsorb Fe^{3+}, but also can capture it, which provides a new platform for the adsorption and removal of Fe^{3+} in aqueous and DMF solutions.

For a clearer comparison between this work and related researches, the Fe^{3+} sensing performance of Tb^{3+} based MOFs is shown in Table 1. The results indicate that the Fe^{3+} sensing performance of the Tb-MOFs in this work is better than most related reports.[30–34]

4. Conclusion

Hollow spherical Tb-MOFs were synthesized under one-pot solvothermal method by using H_2TDC as a competitive and protective agent. Tb-MOFs can be used to detect Fe^{3+} by the luminescence quenching effect with excellent selectivity and sensitivity. The LOD and K_{SV} quenching constant of Tb-MOF for Fe^{3+} in aqueous solution are 2.05 μM and 5.8×10^{-4} M^{-1}, respectively. In DMF, the K_{SV} and LOD are 9.5×10^{-4} M^{-1} and 0.80 μM, respectively. More importantly, this work extends the synthetic strategy and methodic versatility for further development of hollow MOFs, and this method has the advantages of simple operation, mild conditions, high yield, uniform morphology and good stability, and can be applied to trace Fe^{3+} detection.

Conflicts of interest

There are no conflicts to declare.

Acknowledgements

This work was supported by the National Natural Science Foundation of China (51574054), Chongqing Municipal Education Commission (KJZD-M201901102), Chongqing Science and Technology Bureau (cstc2021jcyj-msxmX0493, CSTCCXLJRC201905), the Venture & Innovation Support Program for Chongqing Overseas Returnees (Cx2019092), and Guangzhou Science and Technology Project (202002030053).

References

1 Z. Wang, Y. L. Yang and D. Wang, When hollow multishelled structures (HoMSs) meet metal–organic frameworks (MOFs), *Chem. Sci.*, 2020, **11**, 5359–5368.

2 J. M. Zhou, W. Shi, H. M. Li, H. Li and P. Cheng, Experimental studies and mechanism analysis of high-sensitivity luminescent sensing of pollutional small molecules and ions in Ln_4O_4 cluster based microporous metal–organic frameworks, *J. Phys. Chem. C*, 2014, **118**, 416–426.

3 F. N. Al-Rowaili, A. Jamal, M. S. B. Shammakh and A. Rana, A review on recent advances for electrochemical reduction of carbon dioxide to methanol using MOFs and non-MOFs catalysts; challenges and future prospects, *ACS Sustainable Chem. Eng.*, 2018, **6**, 15895–15914.

4 T. Qiu, S. Gao, Z. Liang, D. Wang, H. Tabassum, R. Zhong and R. Zou, Pristine hollow metalorganic frameworks: design, synthesis and application, *Angew. Chem., Int. Ed.*, 2021, **60**, 17314–17336.

5 J. Zhang, H. Lu, L. Zhang, D. Leng, Y. Zhang, W. Wang, Y. Gao, H. Lu and G. Zhu, Metal–organic framework-derived ZnO hollow nanocages functionalized with nanoscale Ag catalysts for enhanced ethanol sensing properties, *Sens. Actuators, B*, 2019, **291**, 458–469.

6 W. Liu, J. Huang, Q. Yang, S. Wang, X. Sun, W. Zhang, J. Liu and F. Huo, Multi-shelled hollow metal–organic frameworks, *Angew. Chem., Int. Ed.*, 2017, **56**, 5512–5516.

7 H. Lee, W. Cho and M. Oh, Advanced fabrication of metal–organic frameworks: template-directed formation of polystyrene@ZIF-8 core–shell and hollow ZIF-8 microspheres, *Chem. Commun.*, 2012, **48**, 221–223.

8 J. Lee, J. Kwak and W. Choe, Evolution of form in metal–organic frameworks, *Nat. Commun.*, 2017, **8**, 1–8.

9 T. He, S. Chen, B. Ni, Y. Gong, Z. Wu, L. Song, L. Gu, W. Hu and X. Wang, Zirconium–porphyrin-based metal–organic framework hollow nanotubes for immobilization of noble-metal single atoms, *Angew. Chem., Int. Ed.*, 2018, **57**, 3551–3556.

10 L. Peng, J. Zhang, J. Li, B. Han, Z. Xue, B. Zhang, J. Shi and G. Yang, Hollow metal–organic framework polyhedra synthesized by a CO_2-ionic liquid interfacial templating route, *J. Colloid Interface Sci.*, 2014, **416**, 198–204.

11 G. Y. Jeong, R. Ricco, K. Liang, J. Ludwig, J. O. Kim, P. Falcaro and D. P. Kim, Bioactive MIL-88A framework hollow spheres via interfacial reaction in-droplet microfluidics for enzyme and nanoparticle encapsulation, *Chem. Mater.*, 2015, **27**, 7903–7909.

12 L. Yu, J. F. Yang and X. W. Lou, Formation of CoS_2 nanobubble hollow prisms for highly reversible lithium storage, *Angew. Chem., Int. Ed.*, 2016, **55**, 1433–7851.

13 X. Zhang, C. Y. Chuah, P. Dong, Y. Cha and M. K. Song, Hierarchically porous Co-MOF-74 hollow nanorods for enhanced dynamic CO_2 separation, *ACS Appl. Mater. Interfaces*, 2018, **10**, 43316–43322.

14 H. H. Yu, M. Y. Fan, Q. Liu, Z. M. Su, X. Li, Q. Q. Pan and X. L. Hu, Two highly water-stable imidazole-based Ln-MOFs for sensing Fe^{3+}, $Cr_2O_7^{2-}/CrO_4^{2-}$ in a water environment, *Inorg. Chem.*, 2020, **59**, 2005–2010.

15 R. C. Geng, H. X. Tang, Q. J. Ma, L. P. Liu, W. S. Feng and Z. J. Zhang, Bimetallic Ag/Zn-ZIF-8: An efficient and sensitive probe for Fe3+ and Cu2+ detection, *Colloids Surf., A*, 2022, **632**, 127755.

16 L. Guo, Y. Liu, R. M. Kong, G. Chen, Z. Liu, F. L. Qu, L. Xia and W. H. Tan, A metal–organic framework as selectivity regulator for Fe^{3+} and ascorbic acid detection, *Anal. Chem.*, 2019, **91**, 12453–12460.

17 J. H. Wang, M. N. Li, S. Yan, Y. Zhang, C. C. Liang, X. M. Zhang and Y. B. Zhang, Modulator-induced Zr-MOFs diversification and investigation of their properties in gas sorption and Fe^{3+} ion sensing, *Inorg. Chem.*, 2020, **59**, 2961–2968.

18 Y. M. Jo, K. Lim, H. J. Choi, J. W. Yoon, S. Y. Kim and J. H. Lee, 2D metal–organic framework derived co-loading of Co_3O_4 and PdO nanocatalysts on In_2O_3 hollow spheres for tailored design of high-performance breath acetone sensors, *Sens. Actuators, B*, 2020, **325**, 128821.

19 S. W. Sun, J. Z. Wang, G. N. Zhang and Z. L. Liu, A luminescent terbium MOF containing uncoordinated carboxyl groups exhibits highly selective sensing for Fe^{3+} ions, *RSC Adv.*, 2014, **4**, 55252–55255.

20 R. j. F. Bogale, Y. Z. Chen, J. W. Ye, Y. Y. Yang, A. Rauf, L. Y. Duan, P. Tian and G. L. Ning, Highly selective and sensitive detection of 4-nitrophenol and Fe^{3+} ion based on a luminescent layered terbium(III) coordination polymer, *Sens. Actuators, B*, 2017, **245**, 171–178.

21 Z. Zhang, Y. Chen, X. Xu, J. Zhang, G. Xiang, W. He and X. Wang, Well-defined metal–organic framework hollow nanocages, *Angew. Chem., Int. Ed.*, 2014, **126**, 439–443.

22 X. L. Zhou, J. C. Dong, Y. H. Zhu, L. M. Liu, Y. Jiao, H. Li, Y. Han, K. Davey, Q. Xu, Y. Zheng and S. Z. Qiao, Molecular scalpel to chemically cleave metal–organic frameworks for induced phase transition, *J. Am. Chem. Soc.*, 2021, **143**, 6681–6690.

23 J. Zhou, H. Li, H. Zhang, H. Li, W. Shi and P. Cheng, A bimetallic lanthanide metal–organic material as a self-calibrating color-gradient luminescent sensor, *Adv. Mater.*, 2015, **27**, 7072–7077.

24 J. T. Wang, T. F. Xia, X. Zhang, Q. Zhang, Y. J. Cui, Y. Yang and G. D. Qian, A turn-on fluorescent probe for Cd^{2+} detection in aqueous environments based on an imine functionalized nanoscale metal–organic framework, *Chem.–Eur. J.*, 2017, **7**, 54892–54897.

25 Q. S. Zhang, J. Wang, Y. A. M. Kirillov, W. Dou, C. Xu, C. L. Xu, L. Z. Yang, R. Fang and W. S. Liu, A superior luminescent metal–organic framework sensor for sensing trace Al^{3+} and picric acid via disparate charge transfer behaviors, *ACS Appl. Mater. Interfaces*, 2018, **10**, 23976–23986.

26 Y. Su, J. Yu, Y. Li, S. F. Z. Phua, G. Liu, W. Q. Lim, X. Yang, R. Ganguly, C. Dang, C. Yang and Y. Zhao, Versatile bimetallic lanthanide metal–organic frameworks for tunable emission and efficient fluorescence sensing, *Commun. Chem.*, 2018, **12**, 1–13.

27 K. Fan, S. S. Bao, W. X. Nie, C. H. Liao and L. M. Zheng, Iridium(III)-based metal–organic frameworks as multiresponsive luminescent sensors for Fe^{3+}, $Cr_2O_7^{2-}$, and ATP^{2-}in aqueous media, *Inorg. Chem.*, 2018, **57**, 1079–1089.

28 L. L. Ren, Y. Y. Cui, A. L. Cheng and E. Q. Gao, Water-stable lanthanide-based metal–organic frameworks for rapid and sensitive detection of nitrobenzene derivatives, *J. Solid State Chem.*, 2019, **270**, 463–469.

29 M. Xiao and P. R. Selvin, Quantum yields of luminescent lanthanide chelates and far-red dyes measured by resonance energy transfer, *J. Am. Chem. Soc.*, 2001, **123**, 7067–7073.

30 J. F. Guo, M. Y. Zhang, Q. Z. Guo, G. P. Yan and L. J. Liu, Highly stable terbium(III)-based metal–organic framework for the detection of m-dinitroaromatics and Fe^{3+} in water, *Inorg. Chim. Acta*, 2021, **525**, 120454.

31 C. X. Qi, Y. B. Xu, H. Li, X. B. Chen, L. Xu and B. Liu, A highly sensitive and selective turn-off fluorescence sensor for Fe^{3+} detection based on a terbium metal–organic framework, *J. Solid State Chem.*, 2021, **294**, 121835.

32 S. Hussain, X. N. Chen, W. T. A. Harrison, M. R. J. Elsegood, S. Ahmad, S. J. Li, S. Muhammad and D. Awoyelu, Synthesis, crystal structures and photoluminescent properties of one-dimensional europium(III)- and terbium(III)-glutarate coordination polymers, and their applications for the sensing of Fe3+ and nitroaromatics, *Front. Chem.*, 2019, **7**, 728.

33 W. Wang, N. Gong, H. Yin, B. Zhang, P. Y. Guo, B. Liu and Y. Y. Wang, Two stable terbium–organic frameworks based on predesigned functionalized ligands: selective sensing of Fe^{3+} ions and C_2H_2/CH_4 separation, *Inorg. Chem.*, 2019, **58**, 10295–10303.

34 H. H. Yu, J. Q. Chi, Z. M. Su, X. Li, J. Sun, C. Zhou, X. L. Hu and Q. Liu, A water-stable terbium metal–organic framework with functionalized ligands for the detection of Fe^{3+} and $Cr_2O_7^{2-}$ ions in water and picric acid in seawater, *CrystEngComm*, 2020, **22**, 3638–3643.